Oscillatory flow through submerged canopies: 1. Velocity structure

Ryan J. Lowe, Jeffrey R. Koseff, and Stephen G. Monismith

Environmental Fluid Mechanics Laboratory, Department of Civil and Environmental Engineering, Stanford University, Stanford, California, USA

Received 26 October 2004; revised 21 March 2005; accepted 25 May 2005; published 15 October 2005.

[1] Many benthic organisms form very rough surfaces on the seafloor that can be described as submerged canopies. Recent evidence has shown that, compared with a unidirectional current, an oscillatory flow driven by surface waves can significantly enhance biological processes such as nutrient uptake. However, to date, the physical mechanisms responsible for this enhancement have not been established. This paper presents a theoretical model to estimate flow inside a submerged canopy driven by oscillatory flow. To reduce the complexity of natural canopies, an idealized canopy consisting of an array of vertical cylinders is used. The attenuation of the in-canopy oscillatory flow is shown to be governed by three dimensionless parameters defined on the basis of canopy geometry and flow parameters. The model predicts that an oscillatory flow will always generate a higher in-canopy flow when compared to a unidirectional current of the same magnitude, and specifically that the attenuation will monotonically increase as the wave orbital excursion length is increased. A series of laboratory experiments are conducted for a range of different unidirectional and oscillatory flow conditions, and the results confirm that oscillatory flow increases water motion inside a canopy. It is hypothesized that this higher in-canopy flow will enhance rates of mass transfer from the canopy elements, a problem formally investigated in a companion paper (Lowe et al., 2005b).

Citation: Lowe, R. J., J. R. Koseff, and S. G. Monismith (2005), Oscillatory flow through submerged canopies: 1. Velocity structure, *J. Geophys. Res.*, *110*, C10016, doi:10.1029/2004JC002788.

1. Introduction

[2] Water motion is known to have a major affect on sessile benthic organisms by influencing processes such as nutrient uptake, waste removal and larval dispersion. This tight coupling of biological processes with hydrodynamics has been observed for a broad range of benthic organisms such as bivalves [e.g., *Wildish and Kristmanson*, 1997; *Crimaldi et al.*, 2002], coral reef communities [e.g., *Bilger and Atkinson*, 1992; *Thomas and Atkinson*, 1997], kelp [e.g., *Reed et al.*, 1997; *Hurd*, 2000], and seagrasses [e.g., *Koch*, 1994; *Thomas et al.*, 2000]. The vast majority of these studies have focused on the effects of unidirectional flow. However, many of these organisms are exposed to surface waves and it is reasonable to assume that in many cases these biological processes are influenced, and perhaps even dominated by this oscillatory motion. Indeed, there appears to be growing evidence that processes such as nutrient uptake are greatly enhanced by oscillatory flow. For example, *Carpenter et al.* [1991], who studied uptake by coral reef algae, and *Thomas and Cornelisen* [2003], who studied uptake by seagrasses, both found that the rate of nutrient uptake was significantly higher under oscillatory flow when compared to a unidirectional flow of the same magnitude. Similarly, *Hearn et al.* [2001], *Falter et al.* [2004, 2005], and *Reidenbach et al.* [2005] proposed that nutrient uptake by coral reef communities is significantly enhanced by oscillatory motion. To date, however, there have been no direct measurements of any physical mechanism linking oscillatory flow to the enhancement of these biological processes.

[3] Many benthic organisms form very rough surfaces, more often resembling submerged canopies than the typical rough surfaces encountered in engineering literature. For example, Figure 1a shows a photograph of a coral reef community, composed of the coral *Porites compressa*, in Kaneohe Bay, Oahu, Hawaii. The coral form a complex canopy made up of individual, cylindrical branches. For unidirectional flow, several studies have investigated how the particular geometry (morphology) of these coral canopies influences both the flow structure inside the canopy [e.g., *Chamberlain and Graus*, 1975] and the rate at which scalar quantities such as dissolved nutrients are transferred to the tissue of the organism [e.g., *Helmuth et al.*, 1997]. Yet, to our knowledge no comparable literature has investigated how these processes are fundamentally modified by oscillatory flow.

[4] Developing models to predict flow inside natural benthic canopies is an obvious challenge, due to difficulties in incorporating the complexity of the canopy geometry

0148-0227/05/2004JC002788$09.00

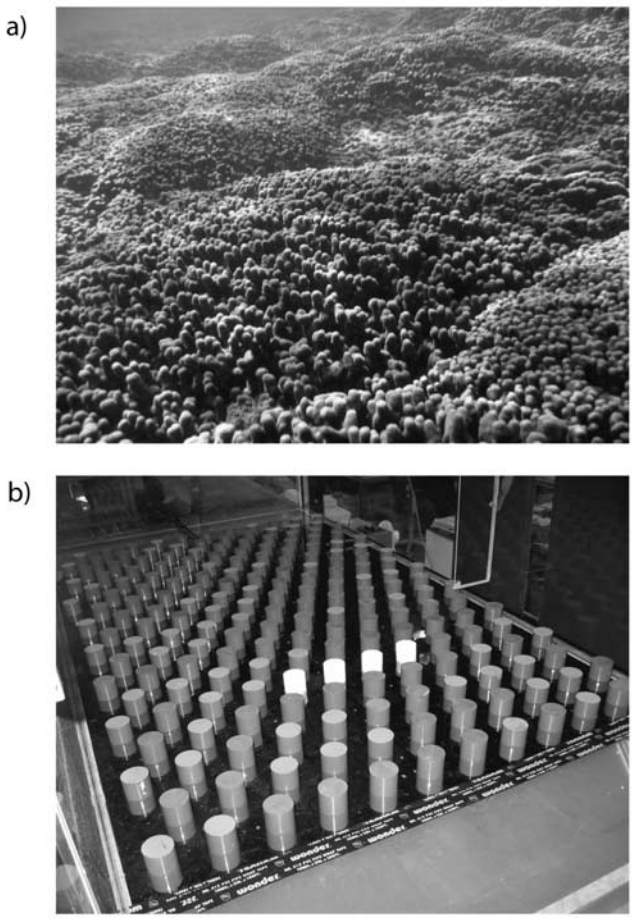

Figure 1. (a) Photo of a pavement of *Porites compressa* in Kaneohe Bay, Oahu, Hawaii and of (b) the model canopy array looking upstream from the trailing edge. The four white cylinders visible are made of gypsum and are only used in the mass transfer experiments detailed in the work of *Lowe et al.* [2005b]. See color version of this figure in the HTML.

(Figure 1a). For these canopies it is impractical to directly model the in-canopy flow, since there is such a broad range of length scales. Instead, it is desirable to simplify the geometry into something more tractable. Perhaps the simplest three-dimensional model of this type of roughness is a submerged canopy composed of an array of vertical cylinders (Figure 1b). For unidirectional flow, idealized canopies such as these have been used to simulate flow through coral branches [e.g., *Chamberlain and Graus*, 1975; *Helmuth et al.*, 1997]. While these simple models do not capture the full complexity of a real canopy, they are used in this study as a first step in understanding how waves interact with these very rough surfaces.

[5] A significant body of literature exists describing unidirectional flow through submerged canopies, and ideas developed in these studies will serve as the foundation for understanding the effects of oscillatory flow. In general, these studies can be broken down into two categories: flow through urban-like roughness [e.g., *Macdonald*, 2000; *Britter and Hanna*, 2003; *Coceal and Belcher*, 2004] and flow through vegetative canopies [e.g., *Nepf and Vivoni*, 2000; *Finnigan*, 2000; *Ghisalberti and Nepf*, 2002]. Many of these studies have measured flow using simple, idealized canopy geometries (e.g., cylinder arrays), such as those described in this paper. Some numerical studies of unidirectional flow through these model canopies have also been reported (e.g., O. Coceal et al., Numerical simulation of turbulent flow over cubic roughness arrays, submitted to *Journal of Fluid Mechanics*, 2004, hereinafter referred to as Coceal et al., submitted manuscript, 2004).

[6] This paper represents the first of two companion papers which investigate how flow (either unidirectional or oscillatory) and canopy geometry parameters influence both the in-canopy velocity structure and mass fluxes to the canopy elements. In this paper, the canopy flow structure is specifically investigated, while in the subsequent paper, *Lowe et al.* [2005b], the mass transfer problem is addressed. Results show that oscillatory flow always enhances flow inside a canopy when compared to a unidirectional current of the same magnitude. The amount of enhancement is found to be a function of both canopy geometry and wave kinematic parameters. These findings have important implications for benthic organisms in the coastal ocean since they suggest that biological processes such as nutrient uptake may often be controlled by surface wave motion rather than the steady component of velocity that has received vastly more attention.

[7] This paper is organized as follows. In section 2, theory which can be used to estimate flow inside a submerged canopy established. A generalized theory for oscillatory flow is first developed and unidirectional flow is treated as a special case where the wave period is infinite. This theory is tested in a series of experiments described in sections 3 and 4. Finally, in section 5 the application of the model to coral reef canopies is discussed and predicts that surface waves will significantly enhance flow within these systems.

2. Oscillatory Canopy Flows

[8] Following ideas developed by *Raupach and Shaw* [1982] for unidirectional canopy flows, for oscillatory flows each velocity component at an arbitrary location and time in a canopy can be decomposed into three parts, by using phase averaging (denoted by an overbar) and horizontal spatial averaging (denoted by angled brackets), e.g., for the u component in the streamwise x direction:

$$u = U + u'' + u', \tag{1}$$

where $U = \langle \overline{u} \rangle$ is the space and phase-averaged velocity, $u'' = \overline{u} - U$ represents spatial variations in the phase-averaged velocity field, and $u' = u - U - u''$ is due to turbulent velocity fluctuations. Note that phase-averaging refers to the averaging of oscillatory flow velocities having common phase [see *Lodahl et al.*, 1998] and the spatial averaging operator is defined such that the averaging volume excludes the solid canopy elements.

[9] For general flow conditions, where a unidirectional current is superimposed onto an oscillatory flow, the velocity field U can be further decomposed as

$$U(z,t) = U_c(z) + U_w(z,t), \tag{2}$$

where U_c is the "steady" component associated with the current and U_w is the "unsteady" component associated with the oscillatory flow [*Grant and Madsen*, 1986]. Throughout this paper the subscript "c" will be used to denote terms associated with a current and the subscript "w" will be used to denote terms associated with the oscillatory flow. It will be shown below that unidirectional flow represents a special solution to the oscillatory canopy flow problem. Hence theory describing oscillatory flow inside the canopy is first developed.

[10] When surface waves propagate over a rough bottom, resistance forces (shear stresses, form drag, etc.) are confined to a finite region near the bed termed the wave boundary layer [*Grant and Madsen*, 1986]. Above the wave boundary layer, the oscillatory velocity field is assumed to be independent of the roughness and described by potential wave theory. Let us define this canopy-independent velocity field $U_{\infty,w}$ as

$$U_{\infty,w}(t) = U_{\infty,w}^{\max}\cos(\omega t), \tag{3}$$

where $U_{\infty,w}^{\max}$ is the velocity amplitude and $\omega = 2\pi/T$ is the radian frequency based on the period of the oscillatory motion T. Note that $U_{\infty,w}$ in equation (3) is defined to be independent of elevation z, which differs from the general surface wave case where the magnitude of $U_{\infty,w}$ decays below the free surface for nonshallow wave conditions [*Dean and Dalrymple*, 1991]. However, for simplicity equation (3) is used to develop the oscillatory flow solution and a discussion of how this solution can be applied to the general surface wave case is given below.

[11] The momentum equation governing U_w in the horizontal x direction, which is valid both within and above the canopy, is

$$\frac{\partial U_w}{\partial t} = -\frac{1}{\rho}\frac{\partial P_w}{\partial x} + \frac{1}{\rho}\frac{\partial \tau_w}{\partial z} - f_w, \tag{4}$$

where P_w is pressure, τ_w is the shear stress and f_w is the canopy resistance term resulting from the force per unit fluid mass inside the canopy that is exerted on the flow by the canopy elements [e.g., *Belcher et al.*, 2003]. Within and near the canopy roughness, the velocity field $U_w(z,t)$ describing the velocity over the full water depth ($z > 0$), will deviate from the free stream value $U_{\infty,w}$ (Figure 2). In order to compare the magnitude of the flow at different heights in the water column, the root mean squared (rms) velocities are introduced as

$$U_w^{rms}(z) = \sqrt{\frac{1}{T}\int_0^T U_w^2 dt} \tag{5}$$

and

$$U_{\infty,w}^{rms} = \sqrt{\frac{1}{T}\int_0^T U_{\infty,w}^2 dt}. \tag{6}$$

Figure 2 shows the assumed form of the velocity profile in which the canopy height is denoted h_c. By definition, the velocity at a sufficient height above the top of the canopy is assumed to be unaffected by the canopy roughness, i.e., $U_w^{rms}(z) = U_{\infty,w}^{rms}$. However, within the canopy and slightly above it, U_w^{rms} is attenuated below the value of $U_{\infty,w}^{rms}$ that would otherwise be obtained by extrapolating into the canopy region.

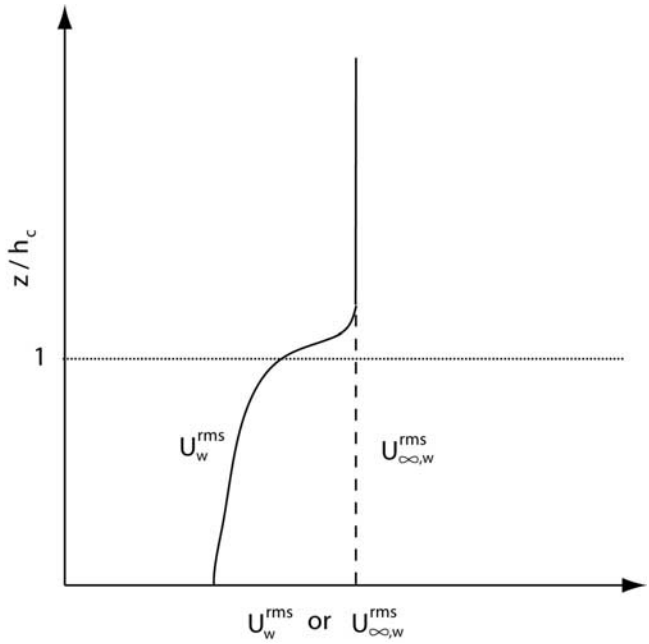

Figure 2. Velocity profiles for oscillatory flow. The solid line represents the rms wave orbital velocity U_w^{rms}. The dashed line represents the rms velocity for potential flow $U_{\infty,w}^{rms}$, which is independent of the canopy roughness. Note that at some height above the canopy, U_w^{rms} and $U_{\infty,w}^{rms}$ overlap.

[12] As illustrated in Figure 2, U_w^{rms} will vary with height inside the canopy. To simplify the problem of modeling flow within the canopy, a representative canopy flow velocity $\widehat{U}_w^{rms}$ is defined as the vertically averaged rms velocity inside the canopy, i.e.,

$$\widehat{U}_w^{rms} = \frac{1}{h_c}\int_0^{h_c} U_w^{rms} dz, \tag{7}$$

where the "overhat" will be used throughout this paper to denote a representative (canopy vertically averaged) term. A canopy attenuation parameter α_w for the oscillatory flow can then be defined as the ratio of the in-canopy velocity to the free-stream velocity

$$\alpha_w \equiv \frac{\widehat{U}_w^{rms}}{U_{\infty,w}^{rms}}. \tag{8}$$

The attenuation parameter α_w provides a quantitative measure of the reduction of the in-canopy velocity from its above-canopy potential flow value.

[13] In order to model flow inside the canopy, the effect of the canopy geometry must be parameterized. The influence of canopy geometry on unidirectional flow has been described in several studies (see reviews by *Finnigan* [2000] and *Britter and Hanna* [2003]). Consider the simple case where the canopy consists of a vertical array of circular

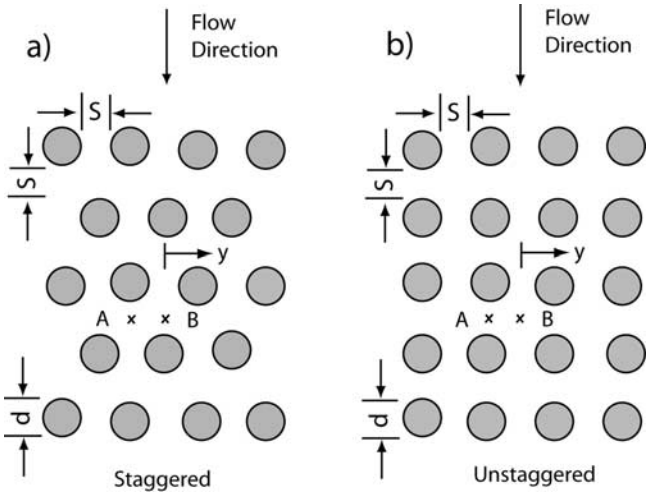

Figure 3. Diagram of the cylinder array geometries: (a) a staggered orientation and (b) an unstaggered orientation.

cylinders separated by a distance S, each of diameter d and height h_c (Figure 3). This is the form of the model canopies used in the experiments detailed below. The particular geometry of the canopy elements is known to determine the flow structure inside the canopy, and its effect is often parameterized using the so-called "lambda parameters" [*Britter and Hanna*, 2003]:

$$\lambda_f = A_f / A_T \tag{9}$$

and

$$\lambda_p = A_p / A_T, \tag{10}$$

where A_f is the canopy element frontal area, A_p is the canopy element plan area, and A_T is the underlying surface area (total area divided by the number of elements). For the cylindrical canopy elements shown in Figure 3, these parameters are: $\lambda_f = h_c d/(S + d)^2$ and $\lambda_p = (\pi d^2/4)/(S + d)^2$.

[14] The canopy flow equation (equation (4)) is valid both within and above the canopy region. Sufficiently high above the canopy (above the wave boundary layer), equation (4) reduces to

$$\frac{\partial U_{\infty,w}}{\partial t} = -\frac{1}{\rho}\frac{\partial P_w}{\partial x}, \tag{11}$$

where $\partial P_w/\partial x$ is the oscillatory pressure gradient driving the flow which from equation (3) is independent of elevation z. Substituting equation (11) into equation (4) to eliminate the pressure gradient term gives

$$\frac{\partial\left(U_w - U_{\infty,w}\right)}{\partial t} = \frac{1}{\rho}\frac{\partial \tau_w}{\partial z} - f_w. \tag{12}$$

To derive an equation governing the in-canopy velocity $\widehat{U}_w$, equation (12) can be integrated over the canopy height (from $z = 0$ to $z = h_c$) and divided by h_c to give

$$\frac{\partial\left(\widehat{U}_w - U_{\infty,w}\right)}{\partial t} = \frac{|u_{*w}|u_{*w}}{h_c} - \widehat{f}_w, \tag{13}$$

where $\widehat{f}_w(t)$ is equal to the depth-averaged canopy resistance force per unit canopy fluid mass and it has been assumed that the stress at the base of the canopy $\tau_w(z = 0)$ is negligible. The time-varying friction velocity $u_{*w}(t)$ is defined as $|u_{*w}|u_{*w} = \tau_w(z = h_c)/\rho$ where $\tau_w(z = h_c)$ is the shear stress at the top of the canopy. Equation (13) will ultimately be used to calculate $\widehat{U}_w$ (and thus α_w) as a function of the canopy geometry and flow conditions. The forcing is provided by $U_{\infty,w}$, which is determined from the known flow conditions per equation (3). However, the stress and resistance force terms on the right side of equation (13) are a function of both the flow conditions and canopy geometry, and these must first be parameterized.

[15] For unidirectional canopy flows, the magnitude of the shear stress is well-known to peak near the top of the canopy and decrease above and below this height [*Finnigan*, 2000]. Accordingly, when the flow is in the positive x direction, the shear stress gradient $\partial\tau_w/\partial x$ above the canopy is locally negative and hence the shear stress term provides a resistance to the above-canopy flow. However, within the canopy region where $\partial\tau_w/\partial x > 0$, this term instead provides a force which drives fluid motion inside the canopy. While several studies have investigated shear stresses generated by unidirectional flow over canopies [e.g., *Kastner-Klein and Rotach*, 2004], no comparable studies have investigated shear stresses generated by oscillatory flow. However, a large body of literature has focused on parameterizing wave-driven shear stresses over arbitrary rough surfaces using a quadratic friction law based on the magnitude of the near-bed orbital velocity [e.g., *Nielsen*, 1992]. Hence for oscillatory flow the magnitude of the shear stress at the top of the canopy $\tau_w(z = h_c)$ can be parameterized using the velocity $U_{\infty,w}$ (equivalent to the near-bed orbital velocity) according to

$$\tau_w(z = h_c) = \rho|u_{*w}|u_{*w} = \frac{1}{2}\rho C_f|U_{\infty,w}|U_{\infty,w}, \tag{14}$$

where C_f is an empirical friction coefficient. Equation (14) will be used to parameterize the shear stress in equation (12). Previous studies of unidirectional flow over canopies have found that $u_*/U_\infty \sim 0.1$ (see review by *Grimmond and Oke* [1999]), which corresponds to $C_f \sim 0.01$. It must be noted that the friction coefficient C_f associated with a rough surface can vary as a function of both the roughness geometry and flow conditions [e.g., *Grimmond and Oke*, 1999; *Poggi et al.*, 2004], and thus may differ between unidirectional and oscillatory flow. For simplicity, in this paper a constant value of C_f is used, although a more sophisticated model could incorporate a variable C_f as a function of the flow conditions and canopy geometry, when detailed measurements of canopy shear stresses resulting from oscillatory flow become available.

[16] The canopy resistance force term $\widehat{f}_w$ represents the force per unit canopy fluid mass exerted on the flow by the canopy elements. For oscillatory flow, the canopy resistance force can be described by the Morison equation [*Dean and Dalrymple*, 1991] which treats the total force as the sum of two forces, namely drag $\widehat{f}_d$ and inertia $\widehat{f}_i$:

$$\widehat{f}_w(t) = \widehat{f}_d(t) + \widehat{f}_i(t). \tag{15}$$

The drag force, which is present in unidirectional flow, results from flow separation that causes the surface pressure distribution around the cylinder to be asymmetric [*Schlichting and Gersten*, 2000]. It can be shown that this canopy drag force is

$$\widehat{f}_d(t) = \frac{C_d \lambda_f}{2h_c(1-\lambda_p)} \left|\widehat{U}_w\right| \widehat{U}_w, \tag{16}$$

where C_d is an empirical "sectional drag coefficient" of order 1 that relates the drag force to the spatially averaged in-canopy velocity [see *Coceal and Belcher*, 2004]. The inertia force $\widehat{f}_i$ is unique to unsteady flows and results from fluid accelerating past the canopy elements. For flow within the canopy, it can be shown that the canopy inertia force is

$$\widehat{f}_i = \left(\frac{C_M \lambda_p}{1-\lambda_p}\right) \frac{\partial \widehat{U}_w}{\partial t}, \tag{17}$$

where C_M is an inertia force coefficient that equals 2 for potential flow around circular cylinders [*Dean and Dalrymple*, 1991]. Note that in the literature it is also common to parameterize the inertia force using an added mass coefficient k_m [*Batchelor*, 1967], which is simply related to the inertia coefficient by $C_M = 1 + k_m$ [*Dean and Dalrymple*, 1991].

[17] Substituting the force parameterizations given in equations (14) through (17) into equation (13) gives an equation governing the oscillatory canopy flow:

$$\frac{\partial\left(\widehat{U}_w - U_{\infty,w}\right)}{\partial t} = \frac{\left|U_{\infty,w}\right| U_{\infty,w}}{L_s} - \frac{\left|\widehat{U}_w\right| \widehat{U}_w}{L_d} - \left(\frac{C_M \lambda_p}{1-\lambda_p}\right) \frac{\partial \widehat{U}_w}{\partial t}, \tag{18}$$

where L_s is a canopy shear length scale defined as

$$L_s \equiv \frac{2h_c}{C_f}, \tag{19}$$

and L_d is a canopy drag length scale defined as [*Coceal and Belcher*, 2004]

$$L_d \equiv \frac{2h_c(1-\lambda_p)}{C_d \lambda_f}. \tag{20}$$

Note that the length scales L_s and L_d provide an indication of the strength of the respective shear and drag forces exerted by the canopy. Thus, for a given velocity, the shear and drag forces exerted by a canopy with small L_s and L_d will be greater than a canopy having large L_s and L_d.

[18] In equation (18) the acceleration terms on the left side are balanced by force terms on the right. Depending on the particular canopy geometry and flow conditions, some of these forces can be neglected. To determine the relative magnitude of each term, a scaling analysis is performed. Each dimensional variable in equation (18), namely $\widehat{U}_w$, $U_{\infty,w}$ and t, is nondimensionalized as a characteristic variable:

$$\widehat{U}_w^* = \frac{\widehat{U}_w}{U_{\infty,w}^{rms}}, \quad U_{\infty,w}^* = \frac{U_{\infty,w}}{U_{\infty,w}^{rms}}, \quad t^* = \omega t. \tag{21}$$

Substituting equation (21) into equation (18) and rearranging gives

$$\frac{\partial\left(\widehat{U}_w^* - U_{\infty,w}^*\right)}{\partial t^*} = \left(\frac{A_\infty^{rms}}{L_s}\right) \left|U_{\infty,w}^*\right| U_{\infty,w}^* - \left(\frac{A_\infty^{rms}}{L_d}\right) \left|\widehat{U}_w^*\right| \widehat{U}_w^* - \left(\frac{C_M \lambda_p}{1-\lambda_p}\right) \frac{\partial \widehat{U}_w^*}{\partial t^*}, \tag{22}$$

in which $A_\infty^{rms} = U_{\infty,w}^{rms}/\omega$ is the rms wave orbital excursion length of the free-stream potential flow. On the right side of equation (22), the shear stress, drag, and inertia force terms are multiplied by the dimensionless parameters: A_∞^{rms}/L_s, A_∞^{rms}/L_d and $(C_M\lambda_p)/(1-\lambda_p)$, respectively. Since the dimensionless (*) variables are all of order one, the magnitude of these parameters determines the relative importance of each term. For certain values of these parameters, simple solutions to equation (22) exist. Some of these cases will now be discussed.

2.1. Canopy Flow Regimes

2.1.1. Canopy Independent Flow

[19] For the simplest case where the canopy density is sufficiently sparse ($\lambda_p \ll 1$) such that the inertia parameter $(C_M\lambda_p)/(1-\lambda_p)$ is small, and A_∞^{rms} is small such that $A_\infty^{rms} \ll L_s$ and $A_\infty^{rms} \ll L_d$, all of the force terms on the right side of equation (22) can be neglected. The flow inside the canopy is governed by potential flow (equation (11)) and is thus not affected by the presence of the canopy elements. For this case the attenuation parameter is

$$\alpha_w = 1. \tag{23}$$

2.1.2. Inertia Force Dominated

[20] For cases where $A_\infty^{rms} \ll L_s$ and $A_\infty^{rms} \ll L_d$, but the inertia parameter $(C_M\lambda_p)/(1-\lambda_p)$ is not negligible, the canopy inertia force is expected to contribute most to the attenuation of the oscillatory canopy flow. A solution for α_w when the flow is inertia dominated, denoted α_i, can be obtained by neglecting the shear and drag force terms and solving equation (22), which gives

$$\alpha_i = \frac{1-\lambda_p}{1+(C_M-1)\lambda_p}. \tag{24}$$

For a canopy, α_i represents the limiting value of α_w as the wave frequency increases, i.e.,

$$\lim_{\omega\to\infty} \alpha_w = \alpha_i. \tag{25}$$

For sparse canopies ($\lambda_p \ll 1$), equation (24) gives $\alpha_i = 1$ and the flow in the canopy is unaffected by the canopy elements, which is consistent with equation (23).

2.1.3. Unidirectional Limit

[21] Equation (22) can be used to predict the velocity inside a canopy for unidirectional flow, by treating this as a special case where the wave period T is infinite. For this case the acceleration terms can be neglected and a force balance is established between the canopy shear stress and drag force terms. Solving equation (22) under these assumptions gives

$$\alpha_c = \sqrt{\frac{L_d}{L_s}}, \tag{26}$$

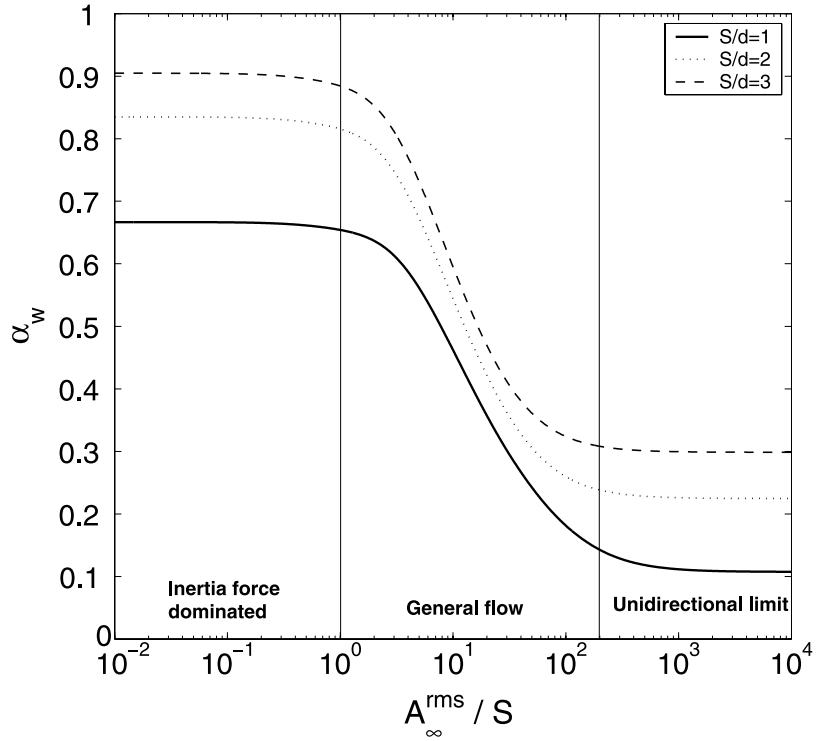

Figure 4. Canopy flow attenuation parameter α_w, calculated by solving equation (22) for the three canopy geometries used in the experiments (Table 3), plotted as a function of the wave orbital excursion length A_∞^{rms}. The three flow regimes are distinguished by the vertical lines.

where α_c represents the attenuation parameter associated with the unidirectional current. A definition of α_c that is equivalent to equation (8) for this unidirectional flow case is

$$\alpha_c \equiv \frac{\widehat{U}_c}{U_{\infty,c}}, \tag{27}$$

where $\widehat{U}_c$ is the representative in-canopy velocity and $U_{\infty,c}$ is the free stream velocity of the current. Equation (26) is a function of the ratio of the canopy drag and canopy shear length scales. Since by definition $\alpha_c < 1$, this implies that this model is only valid for $L_d < L_s$ or specifically $C_f(1 - \lambda_p) < C_d\lambda_f$. As discussed above, C_f is typically two orders of magnitude smaller than C_d, so the model is expected to break down when $\lambda_f \ll 1$, in other words for very sparse canopies. It should be noted that the predicted in-canopy velocity in equation (26) is consistent with the velocity predicted in the model described in the work of *Bentham and Britter* [2003]. Using data compiled from several experiments, *Bentham and Britter* [2003] verified that equation (26) works well to predict the canopy flow velocity when the canopy is sufficiently dense such that $\lambda_f > 0.2$.

[22] The value of α_c in equation (26) represents the value of α_w in the limit as the wave frequency ω approaches zero, i.e.,

$$\lim_{\omega \to 0} \alpha_w = \alpha_c. \tag{28}$$

Hence for a given canopy geometry, α_c is the minimum attainable value of the canopy attenuation parameter. Accordingly, for a given canopy geometry, the attenuation of the oscillatory flow α_w is bounded by the unidirectional and inertia-dominated limits, i.e.,

$$\alpha_c < \alpha_w < \alpha_i. \tag{29}$$

2.1.4. General Flow

[24] In general, it is possible that none of the force terms on the right side of equation (22) can be neglected. For this case, equation (22) is solved numerically (see Appendix 1 for a discussion of the technique). Equation (22) indicates that α_w will be a function of three dimensionless parameters, i.e.,

$$\alpha_w = \alpha_w\left(\frac{A_\infty^{rms}}{L_s}, \frac{A_\infty^{rms}}{L_d}, \frac{C_M\lambda_p}{1-\lambda_p}\right). \tag{30}$$

However, L_s, L_d and $(C_M\lambda_p)/(1 - \lambda_p)$ in equation (30) are determined only by the canopy geometry, since C_f, C_d, and C_M are assumed constant, so for a given canopy α_w is only a function of A_∞^{rms}. Figure 4 shows α_w calculated using equation (22) for the three model canopies used in the experiments described below, plotted as a function of the wave orbital excursion length A_∞^{rms} which is varied over several orders of magnitude. The shape of each curve is similar and three distinct regions are highlighted. In the inertia force dominated region, α_w attains a maximum value where the inertia force term dominates such that $\alpha_w = \alpha_i$, as given by equation (24). Further reducing A_∞^{rms}/S has no effect on α_w. In the opposite limit, when A_∞^{rms}/S is large, a unidirectional flow limit is reached where $\alpha_w = \alpha_c$, as given by equation (26). Finally, in the center region all of the force terms in equation (22) must be considered and α_w depends on the particular value of A_∞^{rms}/S.

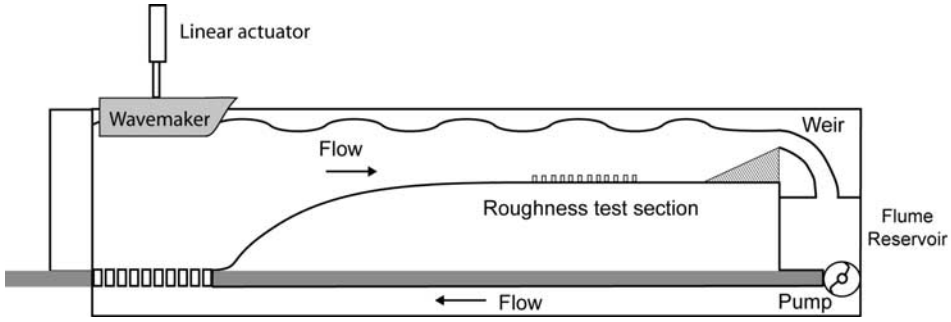

Figure 5. The recirculating wave-current flume and wavemaker used in the experiments.

[25] This example shows that oscillatory flow always enhances the magnitude of the in-canopy flow when compared to a unidirectional flow. The reason for this enhancement can be seen by investigating the sign of each term in equation (22). For unidirectional flow where $A_\infty^{rms}/S \gg 1$, the shear stress term provides the only positive force driving flow inside the canopy. However, for oscillatory flow an extra driving force term ($\partial U_{\infty,w}/\partial t$) exists, which equation (11) shows is equivalent to the oscillatory flow induced pressure gradient. This pressure gradient enhances the in-canopy flow under oscillatory flow conditions.

2.2. Application to Surface Wave Conditions

[26] The model developed above has assumed a free-stream velocity $U_{\infty,w}$ of the form given in equation (3), where $U_{\infty,w}^{\max}$ is uniform with elevation z. However, under general surface wave conditions the potential wave velocity field $U_{\infty,w}$ can vary with z. Specifically, for linear progressive waves the velocity amplitude is [*Dean and Dalrymple*, 1991]

$$U_{\infty,w}^{\max}(z) = a\omega\frac{\cosh(kz)}{\sinh(kh)}, \tag{31}$$

where a is the surface elevation amplitude, h is the water depth, and $k = 2\pi/\lambda$ is the wave number based on the wave length λ. Note that for shallow water waves where $kh \ll 1$, $U_{\infty,w}^{\max}$ is uniform with depth such that the model developed above can be directly applied. However, the model above can also be readily extended to nonshallow wave conditions if $U_{\infty,w}^{\max}$ varies minimally over the height of the canopy h_c. According to equation (31) this will occur when $kh_c \ll 1$, in other words when the height of the canopy is much smaller than the wavelength, a case that frequently exists in practical situations. For this case the free stream velocity $U_{\infty,w}$ can be taken as the velocity measured directly above the canopy (outside the wave boundary layer) and equation (22) can be solved to determine α_w.

3. Experimental Methodology

[27] The experiments were conducted in a recirculating wave-current flume that is 1.2 m wide and 12.5 m long (Figure 5). The test section is 7.32 m long and is constructed of glass, allowing optical access on all sides. Unidirectional flow was driven by a centrifugal pump controlled by a variable frequency drive. For a detailed description of the flume see *Pidgeon* [1999].

[28] Waves were generated at the upstream end of the flume using a plunger-type wavemaker. The wavemaker plunger extends across the width of the tank and is 120 cm long. A servomotor and linear actuator is attached to the top of the wavemaker and its position is controlled by a 0–10 V signal. Surface waves were generated in the direction following the current by sending a sinusoidal voltage signal to the servomotor. A sloping weir was located at the downstream end of the flume to minimize reflection of wave energy, since the flow over the weir is supercritical. Thus, in order to fully minimize the reflection of wave energy, a background current of at least few cm/s was required in all wave experiments.

[29] A Dantec two-component Laser Doppler Anemometer (LDA), operated in forward scatter mode, was used to measure streamwise u and vertical w components of velocity. The laser and LDA optics were placed on a 3-axis motorized traverse that enabled the vertical position of the sampling volume to be positioned to an accuracy of 0.2 mm. For all experiments the flume was filled to a depth h = 43 cm, and velocities were acquired at the following 16 heights above the origin (z = 0) defined at the base of the cylinders: z = 1, 3, 5, 6, 7, 8, 9, 10, 11, 12, 13, 14, 15, 17, 20, 25 cm. These heights were chosen to focus on the flow structure near the top of the canopy elements where the greatest shear in the flow was present. For the unidirectional flow experiments, velocities at each height were acquired continuously at 50 Hz for 20 minutes. For the wave experiments, velocities were acquired at specific phases of the wave synchronized with the wave maker, in order to obtain the mean phase-dependent velocity field. For each sampling point, the velocity was sampled at 20 degree phase increments (18 velocities per wave period) over a total of 600–1000 waves depending on the experiment. To obtain the phase-averaged velocity U_w, each velocity was binned according to its phase and then averaged. The root mean squared velocity U_w^{rms} was then calculated using equation (5).

[30] The model canopies were constructed using arrays of vertically mounted circular cylinders. Each cylinder was made from PVC rod and had diameter d = 5 cm and height h_c = 10 cm. The cylinder array covered the full width of the tank (1.2 m) and a length 1.8 m in the streamwise direction. During these experiments, three cylinder spacings S were used (Figure 3): S = 5, 10 and 15 cm. Experiments were also conducted to investigate the effect of roughness geometry using staggered and unstaggered orientations (Figure 3). A photo of the cylinder array with S = 5 cm and a staggered

Table 1. Parameters for the Unidirectional Flow Experiments

Run	Geometry	S/d	$U_{\infty,c}$, cm/s	$u_{*c}/U_{\infty,c}$	C_f	α_c
U1	staggered	1	4.8	0.10	0.019	0.12
U2	staggered	1	9.2	0.09	0.017	0.10
U3	staggered	1	12.4	0.10	0.018	0.10
U4	staggered	2	4.5	0.12	0.031	0.22
U5	staggered	2	9.1	0.12	0.030	0.23
U6	staggered	3	4.3	0.13	0.032	0.32
U7	staggered	3	8.5	0.12	0.029	0.33
U8	unstaggered	1	4.4	0.09	0.018	0.12
U9	unstaggered	1	9.4	0.09	0.017	0.11

orientation is shown in Figure 1b. It should be noted that a spacing $S = 5$ cm was the smallest spacing that could be used, since further reducing the spacing would obstruct the laser beams.

[31] The flow conditions and cylinder array properties used in the experiments are summarized in Tables 1 and 2. These comprised a total of 9 unidirectional flow experiments (U1–U9) and 16 wave experiments (W1–W16). In all experiments velocity profiles were collected at a distance $x \approx 1.3$ m downstream of the leading edge of the canopy near the flume centerline at $y = 0$, except in a few experiments where the streamwise development of flow inside the canopy was specifically investigated. As discussed in section 2, the velocity field inside a canopy varies with horizontal position in the canopy, but the velocity of interest in this study is the spatially averaged velocity $U(z)$. To investigate these spatial variations, for each flow condition two separate velocity profiles were collected at the following horizontal locations in the canopy (see Figure 3): 1) directly behind a cylinder (point A), and in an open region (point B). To an approximation $U(z)$ will be assumed to be the average of the profiles measured at points A and B.

4. Results

4.1. Unidirectional Flow

[32] A total of nine unidirectional flow experiments (denoted U1–U9) were conducted using the flow conditions and cylinder spacings listed in Table 1. It should be noted that the free stream velocity $U_{\infty,c}$ cited in these experiments is assumed to be represented by the velocity measured at $z/h_c = 2.5$, the maximum height of the LDA traverse. This assumes that the velocity above this height is uniform which is not strictly the case. However, in two experiments (U2 and U7), an acoustic Doppler velocimeter was used to measure the mean velocity profile at roughly 3 cm intervals from $z/h_c \approx 1.3$–3.7. These measurements showed that the velocity was mostly uniform above $z/h_c = 2.5$ and thus using the velocity measured at $z/h_c = 2.5$ to estimate the actual free stream velocity $U_{\infty,c}$ is expected to induce less than a 10% error.

4.1.1. Flow Development and Cross-Stream Inhomogeneities

[33] A series of velocity profiles were collected for experiment U1, at several distances x downstream of the leading edge of the canopy, to investigate the development of the in-canopy flow. All of these profiles were measured at point B, in an open region. *Belcher et al.* [2003] showed that the velocity inside the canopy will develop over a distance from the leading edge of the canopy (located at $x = 0$) that is on the same order as the canopy drag length scale L_d defined in equation (20). However, to calculate L_d the sectional drag coefficient C_d must be specified, which is difficult to directly measure. *Coceal and Belcher* [2004], however, evaluated data from several experiments and found that $C_d = 2$–3. This range of values was recently confirmed in direct numerical simulations reported by Coceal et al. (submitted manuscript, 2004). At first glance this value of C_d may be viewed as higher than other drag coefficient values reported in the literature that tend to be closer to 1. In fact, studies typically describe the drag coefficient decreasing from its value in isolation ($\approx$1.2 at these Reynolds numbers) as the canopy element spacing decreases, due to sheltering by upstream elements [e.g., *Brunet et al.*, 1994]. However, as detailed in *Macdonald* [2000] and *Coceal and Belcher* [2004], this apparent discrepancy arises from the use of different reference velocities in the definition of the drag coefficient. For example, it is common to define the drag coefficient C_{dh} based on a reference velocity measured at the top of the canopy $z = h_c$ [e.g., *Cheng and Castro*, 2002; *Ghisalberti and Nepf*, 2004]. The "sectional drag coefficient" C_d used in this paper is referenced to the spatially averaged in-canopy velocity and will thus be higher than C_{dh} since the flow inside the canopy is attenuated. Since the canopy geometries and Reynolds numbers used in this study are similar to the values of these parameters in the experiments described in *Coceal and Belcher* [2004], values of C_d are also expected to be similar. Therefore throughout this paper it will be assumed that $C_d = 2.5$, although in the future a varying value of C_d could be included when detailed studies become available which more accurately relate C_d to the particular canopy geometry and flow conditions.

[34] Figure 6 shows the development of the velocity field measured within and above the canopy, where the downstream distance x is normalized by L_d. For this canopy spacing ($S/d = 1$), L_d was calculated using equation (20) and was $L_d = 13$ cm (Table 3). Initially, at $x/L_d = 0.6$ the velocity profile has a smooth-wall logarithmic shape all the way to the bed. By $x/L_d = 1.3$ the velocity inside the canopy decreases considerably, and progressively decreases further downstream. At $x/L_d = 5.2$ the velocity profile inside the canopy has become fully developed, indicating that the

Table 2. Parameters for the Oscillatory Flow (Wave) Experiments

Run	Geometry	S/d	$U_{c,\infty}$, cm/s	α_c	T, s	$U^{rms}_{\infty,w}$, cm/s	A^{rms}_{∞}/S	α_w	α_w[a]
W1	staggered	1	4.7	0.10	1	2.4	0.08	0.69	0.66
W2	staggered	1	4.6	0.11	2	4.8	0.30	0.70	0.66
W3	staggered	1	4.9	0.08	3	3.5	0.34	0.70	0.66
W4	staggered	1	12.3	0.10	1	2.0	0.06	0.69	0.66
W5	staggered	1	12.7	0.11	2	3.1	0.20	0.72	0.66
W6	staggered	1	9.8	0.08	3	2.2	0.21	0.71	0.66
W7	staggered	2	4.8	0.23	1	2.3	0.04	0.89	0.83
W8	staggered	2	4.9	0.24	2	5.2	0.17	0.90	0.83
W9	staggered	2	4.9	0.22	3	3.4	0.16	0.88	0.83
W10	staggered	2	9.1	0.25	2	3.7	0.12	0.87	0.83
W11	staggered	3	12.0	0.33	1	2.5	0.03	0.92	0.90
W12	staggered	3	4.7	0.35	2	5.3	0.11	0.96	0.90
W13	staggered	3	4.6	0.33	3	3.4	0.11	0.94	0.90
W14	staggered	3	8.8	0.35	2	3.2	0.07	0.92	0.90
W15	unstaggered	1	4.8	0.12	2	3.8	0.22	0.73	0.66
W16	unstaggered	1	10.1	0.14	2	3.6	0.23	0.73	0.66

[a]Predicted value from equation (22).

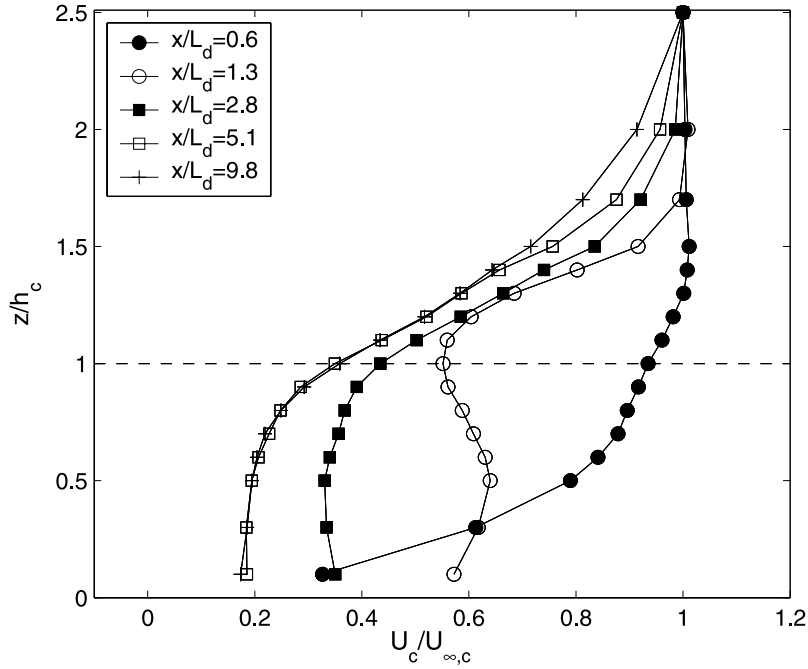

Figure 6. Canopy flow development for experiment U1 at five downstream distances x from the leading edge of the canopy (at $x = 0$). The dashed line indicates the height of the canopy.

adjustment length x_o falls somewhere between $3L_d$–$5L_d$. *Coceal and Belcher* [2004] present a simple model to estimate this adjustment length:

$$x_o \approx 3L_d \ln\left(\frac{U_c(z = h_c)}{u_{*c}} \frac{h_c}{L_d}\right), \tag{32}$$

where $U_c(z = h_c)$ is the mean velocity at the top of the canopy and u_{*c} is the friction velocity. Substituting the measured values of these variables into equation (32) gives $x_o/L_d = 3.1$, where u_{*c} is estimated from the measured Reynolds stress profiles discussed below. This predicted value is consistent with the observed adjustment length of $x_o/L_d = 3$–5 and supports the assumption that $C_d = 2.5$ accurately parameterizes the canopy drag force. For all experiments shown in Tables 1 and 2, velocity profiles were collected at a distance sufficiently far downstream that the velocity field inside the canopy is expected to be fully developed.

[35] To investigate spatial variations in the canopy flow structure, Figure 7 shows a cross-stream velocity profile $(u'')_c$ measured at the midcanopy height ($z = h_c/2$) for experiment U2, located where the in-canopy flow was fully developed ($x = 1.3$ m). Note that the "double prime" notation indicates that the velocity is defined as the time-averaged deviation from the spatially averaged velocity U_c per equation (1). The centers of the cylinders are located upstream of the measurement profile at cross-stream positions $y/d = \pm 1$ (Figure 3). Depending on the particular cross-stream location inside the canopy, $(u'')_c$ is shown to be sinusoidal and vary between ±10% of the free stream velocity $U_{\infty,c}$. The velocity attains a maximum in the open regions $y/d = -2, 0, 2$ at point B (Figure 3). Similarly, there is a velocity minimum directly behind a cylinder $y/d = \pm 1$ at point A. Velocities measured at points A and B thus bound the possible range of velocities along the profile, and moreover, to a good approximation the spatially averaged velocity $U_c(z)$ can be estimated by averaging the velocity profiles measured at points A and B, since the average of $(u'')_c$ at these two points is approximately zero. Although averaging velocities at A and B well approximates the spatially averaged velocity in these experiments where S/d is relatively small, for cases where S/d is large this approximation will be less accurate since the width of the cylinder wakes will become narrow relative to the spacing S, making cross stream profiles of $(u'')_c$ less sinusoidal.

4.1.2. Velocity Structure

[36] Figure 8a shows spatially averaged velocity profiles $U_c(z)$ collected for three different cylinder spacings, corresponding to experiments U2, U5 and U7. For all spacings, U_c inside the canopy is significantly attenuated from the free stream value $U_{\infty,c}$. The velocity inside the canopy is shown to increase as the cylinder spacing is increased, confirming that the canopy flow structure is a strong function of the canopy geometry. For each experiment, an estimate of the representative canopy flow velocity $\widehat{U}_c$ can be determined by numerically integrating the measured in-canopy velocity. An estimate for the canopy attenuation parameter α_c can then be calculated using equation (27) (Table 1). The estimated uncertainties in α_c,

Table 3. Canopy Geometry Parameters and Predicted Values of α_c and α_i, for the Three Cylinder Spacings S Used in the Experiments

S/d	λ_f	λ_p	L_s, cm	L_d, cm	α_c[a]	α_i[b]
1	0.50	0.20	1100	13	0.11	0.67
2	0.22	0.09	660	33	0.22	0.83
3	0.13	0.05	660	58	0.30	0.90

[a]Value calculated using equation (26).
[b]Value calculated using equation (24).

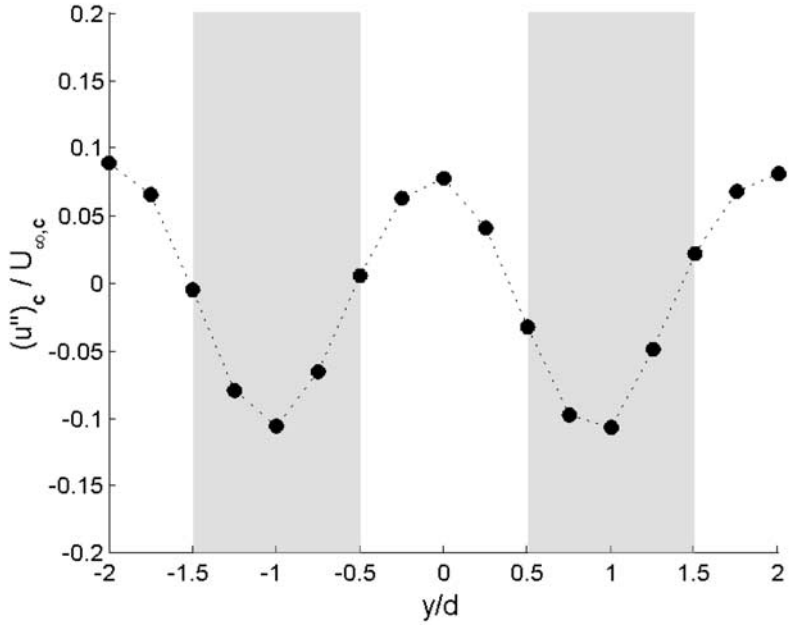

Figure 7. Cross-stream profile (measured at $z/h_c = 0.5$) of the deviation from the spatially averaged velocity $(u'')_c$ for experiment U2 with $S/d = 1$. The velocities are normalized by the free stream velocity $U_{\infty,c}$. For this experiment the centers of the cylinders were located directly upstream at $y/d = \pm 1$. The gray areas denote regions where a cylinder is located immediately upstream.

which were dominated by the uncertainties in estimating $U_{\infty,c}$, were 0.01, 0.02, and 0.03 for experiments with $S/d = 1$, 2 and 3, respectively. Therefore, for a given cylinder spacing, α_c is constant within the margin of error over the full range of flow conditions used in these experiments. Moreover, comparison of the unstaggered geometry experiments (U8–U9) with the staggered experiments at the same cylinder spacing (U1–U3), reveals that α_c agrees within the margin of error for these different cylinder orientations. In these experiments α_c can thus be treated as only a function

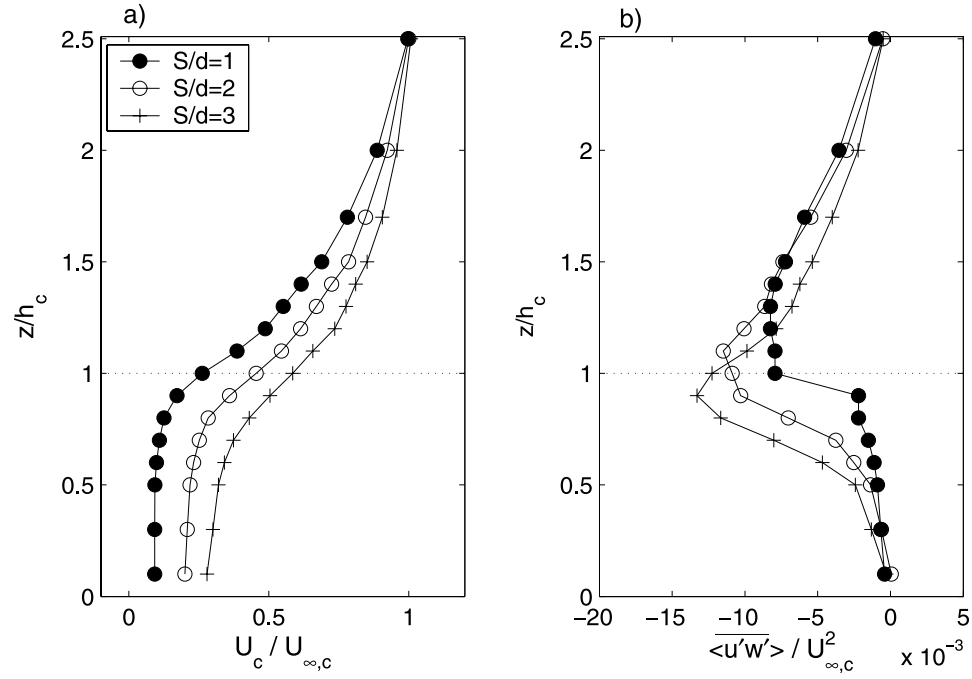

Figure 8. Effect of cylinder spacing on (a) the mean velocity U_c and (b) Reynolds stress profiles $\langle \overline{u'w'} \rangle$ for three different cylinder spacings. $S/d = 1$, experiment U2; $S/d = 2$, experiment U5; $S/d = 3$, experiment U7.

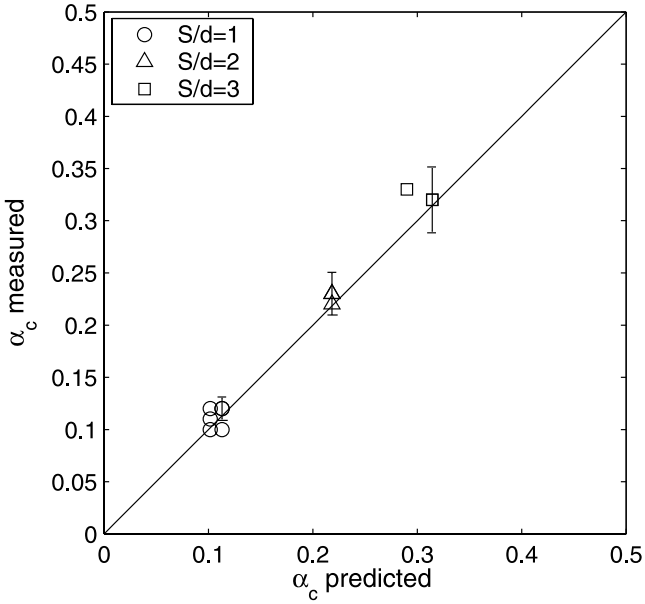

Figure 9. Measured α_c versus that predicted using equation (26) for the unidirectional flow experiments listed in Table 1. Symbols denote the canopy spacing S for the experiment. One representative error bar has been included for each spacing to denote the measurement uncertainty at that spacing.

of the cylinder spacing. The average values of α_c for the three cylinder spacings are: 1) $\alpha_c = 0.11 \pm 0.01$ for $S/d = 1$, 2) $\alpha_c = 0.23 \pm 0.02$ for $S/d = 2$, and 3) $\alpha_c = 0.33 \pm 0.03$ for $S/d = 3$.

[37] Although the turbulence structure is not the focus of this paper, for the unidirectional flow experiments the turbulence measurements will be discussed since they can be used to estimate the canopy shear stress. For unidirectional flows the shear stress is $\tau_c = -\rho\langle\overline{u'w'}\rangle$ where $\langle\overline{u'w'}\rangle$ is the spatially averaged Reynolds stress. Note that the "dispersive stress" resulting from spatial velocity correlations inside the canopy is neglected since it is generally found to be much smaller than the Reynolds stress [*Kastner-Klein and Rotach*, 2004]. Reynolds stress profiles are shown for the three different spacings in Figure 8b. At each spacing the Reynolds stress peaks near the top of the canopy and decreases above and below this height, which is a characteristic of unidirectional canopy flows [see *Finnigan*, 2000]. It is possible to use these Reynolds stress profiles to estimate a friction velocity $u_{*c} \approx \sqrt{-\langle\overline{u'w'}\rangle}$, which characterizes the stress exerted by the canopy onto the overlying flow. The friction velocity for each flow condition was estimated based on the peak value in the Reynolds stress profile [e.g., *Kastner-Klein and Rotach*, 2004] and values for each experiment are listed in Table 1. For these experiments $u_{*c}/U_{\infty,c} \approx 0.1$ which is comparable to values cited in other unidirectional canopy flow studies [e.g., *Grimmond and Oke*, 1999]. Using the estimates of u_{*c} for each experiment, values for the friction coefficient can then be calculated as $C_f = 2u_{*c}^2/U_{\infty,c}^2$ (Table 1). Notably, C_f is a weak function of the canopy geometry, consistent with other observations [see *Grimmond and Oke*, 1999]. This suggests that the structure of the shear layer which forms at the top of the canopy is slightly different for each cylinder spacing [*Poggi et al.*, 2004]. This is supported by Figure 8b, which shows that the peak Reynolds stress migrates slightly vertically as the cylinder density changes.

[38] Figure 9 shows the attenuation parameter α_c measured for each experiment, plotted as a function of the predicted value calculated using equation (26). Note that in the prediction of α_c using the model (equation (26)), the measured value of C_f listed in Table 1 was used to determine L_s. However, a value of $C_d = 2.5$ was used to calculate L_d since it could not be measured directly, which represents the value recommended by *Coceal and Belcher* [2004]. Overall, there is very good agreement between the measured and predicted values of α_c for all cylinder spacings and flow conditions.

4.2. Oscillatory Flow

[39] A total of 16 oscillatory flow experiments (denoted W1–W16) were conducted (Table 2). As noted above, for each wave experiment, a background current was required to minimize upstream reflection of wave energy. The background current $U_c(z)$ was assumed to be the steady component of the velocity field, by treating it as the time-averaged velocity over the duration of the measurement period. For each wave experiment the free-stream current velocity $U_{\infty,c}$, measured at $z/h_c = 2.5$, is listed in Table 2.

[40] The measured current profiles U_c were used to calculate $\widehat{U}_c$ and the attenuation parameter α_c was then calculated using equation (27) (Table 2). For the oscillatory flow experiments, α_c is found to be independent of $U_{\infty,c}$ within experimental error, as was found to be the case for the pure unidirectional flow experiments (U1–U9). Moreover, for a given cylinder spacing, the values of α_c obtained in the wave affected experiments (W1–W16) are roughly the same as the values of α_c measured in the pure unidirectional experiments (U1–U9) at the same canopy spacings. The average values of α_c for the three cylinder spacings used in the wave experiments are: 1) $\alpha_c = 0.10 \pm 0.01$ for $S/d = 1$, 2) $\alpha_c = 0.24 \pm 0.02$ for $S/d = 2$, and 3) $\alpha_c = 0.34 \pm 0.03$ for $S/d = 3$. The fact that α_c is found to be independent of the background wave field indicates that possible current-wave interactions in these experiments are negligible. However, in general this may not always be the case, particularly for cases where the wave velocities are much larger than the current, since wave boundary layer theory predicts that waves can interact with the current through nonlinear interactions to increase the apparent roughness of the bed [*Grant and Madsen*, 1986].

[41] The focus of the oscillatory flow experiments was ultimately on the structure of the unsteady (wave) velocity component $U_w(z,t)$. To investigate how accurately the simple spatial averaging procedure employed in this study predicts the actual spatially averaged value for oscillatory flow, cross-stream variations in the oscillatory velocity structure $(u'')_w^{rms}$ were measured for three wave experiments (W2, W3 and W12). Figure 10 shows a cross-stream profile of $(u'')_w^{rms}$ measured at $z = h_c/2$ for experiment W2. In general, for all wave experiments in which cross-stream measurements were collected, no significant variation in $(u'')_w^{rms}$ was apparent along the profile line. The maximum velocity deviation $(u'')_w^{rms}$ was less than 1% of $U_{\infty,w}^{rms}$. This is markedly different from observations of significant cross-

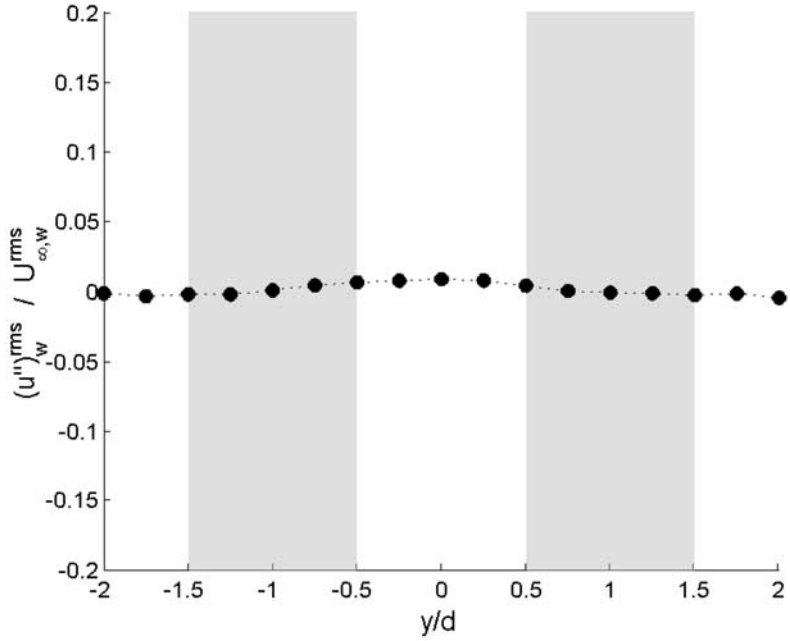

Figure 10. Cross-stream profile (measured at $z/h_c = 0.5$) of the deviation from the spatial averaged rms oscillatory flow velocity $(u'')_w^{rms}$ for experiment W2 with $S/d = 1$. The gray areas denote regions where a cylinder is located immediately upstream.

stream variations in the current structure for unidirectional flow $(u'')_c$ (Figure 7).

[42] For each wave experiment a profile of $U_w^{rms}(z)$ was measured. Figure 11 shows example profiles of U_w^{rms} measured for experiments W2 and W12. In order determine the canopy attenuation parameter α_w using equation (8), the free-stream velocity $U_{\infty,w}$ must be specified. However, according to equation (31), for surface waves the magnitude of the wave orbital velocity can change with elevation z, which will be independent of the canopy roughness. The model developed in section 2 was based on a depth uniform $U_{\infty,w}$, and section 2.2 explained that this model can be

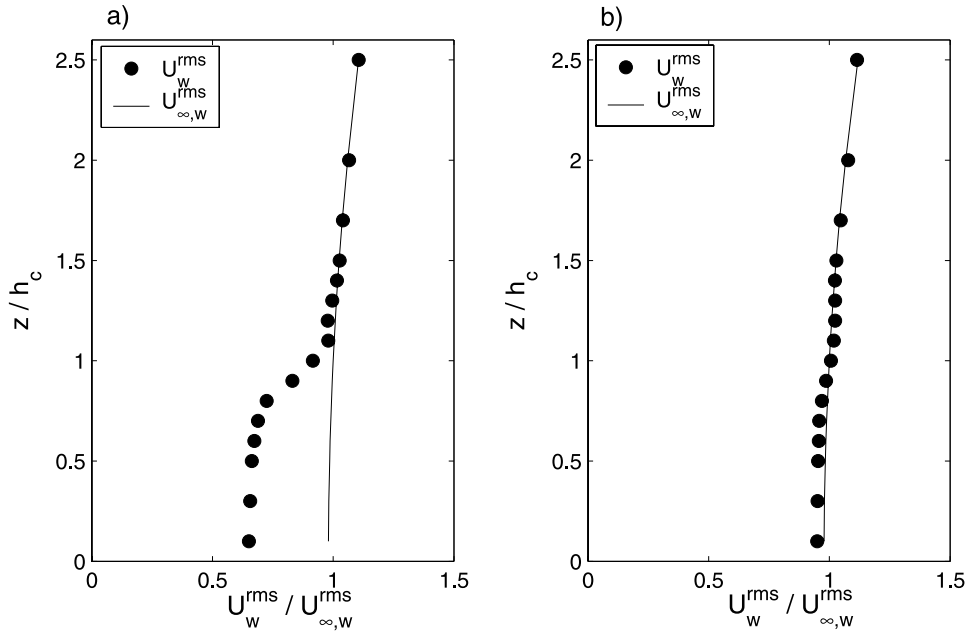

Figure 11. Comparison of the measured rms oscillatory flow velocity U_w^{rms} (indicated by the dots) with the expected potential flow field $U_{\infty,w}^{rms}$ extrapolated into the canopy region (indicated by the solid line) using the fitting procedure in equation (33). (a) Experiment W2 ($S/d = 1$) and (b) experiment W12 ($S/d = 3$).

Table 4. Geometric Parameters of Branched Reef Corals and the Estimated In-Canopy Flow Using the Model Detailed in Section 2[a]

Source	Coral Species	mm						α_w/α_c for A_∞^{rms} =		
		d	S	h_c	λ_p	λ_f	α_i/α_c	1 cm	10 cm	100 cm
Chamberlain and Graus [1975]	Oculina diffusa	5	25	75_a	0.02	0.42	7.0	7.0	5.9	3.0
	Seriatopora hysterix	4	8	50_a	0.09	1.39	11.6	11.3	7.7	3.3
Lesser et al. [1994]	Pocillopora damicornis	6	6	35_a	0.20	1.58	10.4	10.2	7.4	3.2
Marshall [2000]	Acropora formosa	16	37	180	0.07	1.02	10.2	10.0	7.3	3.2
	Acropora humilis	16	11	58	0.28	1.27	8.3	8.3	6.6	3.1
	Acropora palifera	36	25	84	0.27	0.81	6.8	6.7	5.8	3.0
	Pocillopora damicornis	14	8	75	0.32	2.18	10.4	10.2	7.4	3.2
	Porites cylindrica	25	13	99	0.34	1.72	8.9	8.8	6.8	3.2
	Seriatopora hystrix	5	3	81	0.31	6.31	17.8	16.2	9.0	3.4
	Stylophora pistillata	15	11	85	0.26	1.88	10.4	10.2	7.4	3.2
Reidenbach et al. [2005]	Stylophora pistillata	7	16	65_a	0.08	0.86	9.2	9.1	7.0	3.2
	Pocillopora verrucossa	11	14	65_a	0.14	1.10	9.5	9.3	7.1	3.2
	Porites compressa	18	18	75_a	0.38	2.00	9.0	8.9	6.9	3.2

[a]Branch lengths were not listed in this study and were assumed to be equal to half the colony height.

extended to surface waves by using the value of $U_{\infty,w}$ evaluated at the canopy height h_c provided kh_c is small, which is the case in these experiments.

[43] However, slightly above the canopy roughness a wave boundary layer can form where the local velocity can significantly deviate from the potential velocity $U_{\infty,w}$ required to calculate α_w [*Grant and Madsen*, 1986]. In order to most accurately estimate the value of $U_{\infty,w}$ at $z = h_c$ the following approach was implemented. From wave boundary layer theory, a phase lag is known to exist between the flow inside the wave boundary layer and the region above governed by potential flow [see *Nielsen 1992*], and this idea was used to estimate the wave boundary layer thickness. For each experiment, to estimate the wave boundary layer thickness the measured phase lag between the velocity measured at $z/h_c = 2.5$ and the other sampling heights was calculated. For all cases the top of the wave boundary layer was located below $z/h_c = 1.5$, so for each wave experiment, velocities measured at heights $z/h_c = 1.5$, 1.7, 2.0 and 2.5 were assumed to be governed by potential flow. The theoretical potential wave velocity field over the full water column was then determined using nonlinear curve fitting to fit these four velocities to the function

$$U_{\infty,w}^{rms} = a\cosh(bz) \tag{33}$$

where a and b are constants and the cosh dependence is based on the assumed form of the velocity field in equation (31). Example profiles of $U_{\infty,w}^{rms}(z)$ obtained using this fitting procedure for experiments W2 and W12, are indicated by the solid line in Figure 11. These profiles demonstrate why the oscillatory canopy flow model based on a depth uniform free stream velocity can be accurately applied to surface waves when kh_c is small. In these experiments kh_c is small (order 0.1) and as a consequence the theoretical profile of $U_{\infty,w}^{rms}(z)$ in Figure 11 (refer to solid line) changes minimally in the canopy region (from $z = 0$ to h_c) such that the velocity over the full canopy depth can be well approximated by its value at $z = h_c$.

[44] Given the measured profile of U_w^{rms} and the value of $U_{\infty,w}^{rms}$ at $z = h_c$, the attenuation parameter α_w can be calculated by applying equation (8). For each experiment, the calculated value of α_w is listed in Table 2. The estimated measurement uncertainty for α_w is 0.03, which was dominated by errors induced by using the fitted velocity profile to estimate the relevant free stream velocity $U_{\infty,w}^{rms}$, as revealed via Monte Carlo simulations. For the range of wave conditions in these experiments, α_w was found to vary only according to canopy spacing within the measurement uncertainty, as was the case for the unidirectional experiments. The average values of α_w for the three cylinder spacings are: 1) $\alpha_w = 0.71 \pm 0.03$ for $S/d = 1$, 2) $\alpha_w = 0.89 \pm 0.03$ for $S/d = 2$, and 3) $\alpha_w = 0.94 \pm 0.03$ for $S/d = 3$. Comparison of the range of α_w (0.71–0.94) with the range of α_c (0.11–0.33), shows that oscillatory flow significantly enhances flow inside these canopies by 3 to 7 times depending on the cylinder spacing. This is consistent with the theory developed in section 2 which showed that for a given canopy, α_c represents the minimum value of the attenuation parameter α_w, and that oscillatory flow will always increase this value. It was further shown that for a given canopy geometry the attenuation parameter α_w can be a function of the wave orbital excursion length scale A_∞^{rms}. Thus, for each of the three canopy spacings used in these experiments, equation (22) can be solved to predict α_w as a function of A_∞^{rms} for the canopies used in these experiments. These calculations were shown earlier in Figure 4. For each canopy spacing, α_w exhibits three distinct regions. For $A_\infty^{rms}/S < 1$, the flow inside the canopy will be dominated by the inertia force such that $\alpha_w = \alpha_i$, where α_i can be predicted using equation (24). For $A_\infty^{rms}/S > 100$, the canopy flow reaches a unidirectional limit such that $\alpha_w = \alpha_c$, where α_c can be predicted using equation (26). For $1 < A_\infty^{rms}/S < 100$, α_w varies with A_∞^{rms}/S.

[45] Owing to constraints presented by the wavemaker and flume, the range of A_∞^{rms}/S used in the oscillatory flow experiments was 0.03–0.34 (see Table 2). Therefore, based on Figure 4, for all oscillatory flow experiments the in-canopy flow is expected to be dominated by the canopy inertia force such that $\alpha_w \approx \alpha_i$. This explains why for oscillatory flow, α_w was not sensitive to changes in A_∞^{rms}/S even though it was varied by roughly an order of magnitude in the experiments. For each cylinder spacing, α_i was calculated using equation (24) (Table 3). For comparison, α_w is directly calculated by solving equation (22) and these values listed in Table 2 differ negligibly from α_i confirming that for these experiments the flow should be inertia force dominated. Finally, in Figure 12 the values of α_w measured in the experiments are compared to the predicted values of α_w by solving equation (22). In general there is good agreement between the measured and predicted values of α_w although the measured values were always slightly

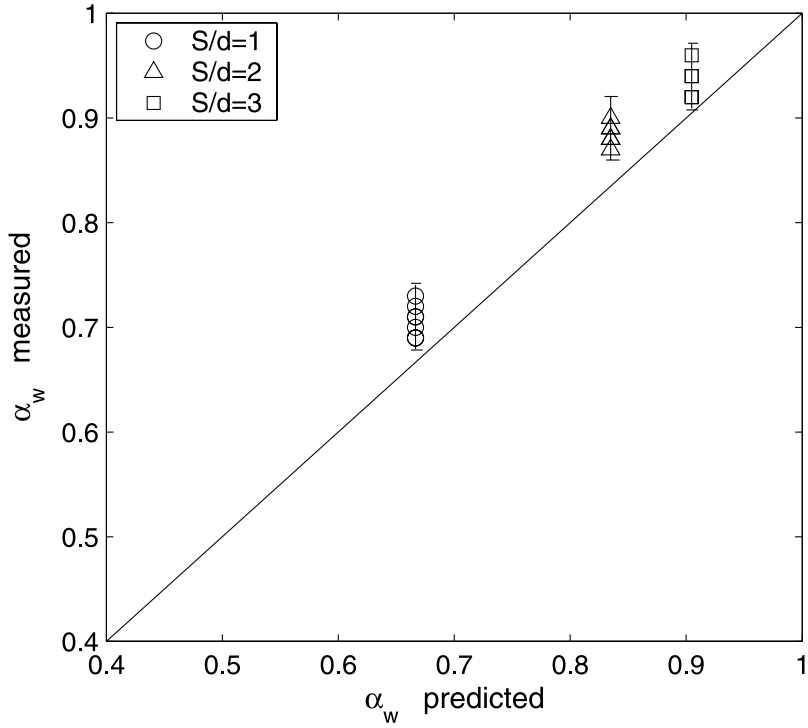

Figure 12. Measured α_w versus that predicted by solving equation (22) for the oscillatory flow experiments listed in Table 2. Symbols denote the canopy spacing S of the experiment. One representative error bar has been included for each spacing to denote the measurement uncertainty at that spacing.

higher (from 5 to 10%) than the predicted values for all cylinder spacings and flow conditions. A possible explanation for this underprediction is that the inertia force coefficient C_M may in fact be smaller than 2 since this value specifically describes two-dimensional flow around cylinders. Since the cylinders are of finite length, the oscillatory flow will be three-dimensional near the top of the canopy which would effectively reduce C_M. For three-dimensional flow around spheres, for example, $C_M = 1.5$. If the value of C_M is reduced from 2 to 1.7, for example, the agreement between the predicted and measured flow is excellent and thus may at least partially explain this underprediction.

5. Application: Coral Reef Canopies

[46] Results have shown that oscillatory flow has the ability to significantly increase water motion inside submerged model canopies when compared to unidirectional flow. However, this study used a relatively limited range of wave conditions and canopy geometries so it is worth investigating whether this oscillatory flow enhancement is expected to be significant within natural benthic canopies exposed to field wave conditions. As an example we consider flow through branched reef corals, as shown earlier in Figure 1a. Although the geometry of these coral canopies is often much more complicated that the simple cylinder arrays used in this study, these corals often have well-defined branch diameters d, spacings S, and lengths h_c, such that the model developed in section 2 can be conveniently applied. Moreover, several studies have tabulated these geometric parameters for a range of different coral species, some of which are listed in Table 4.

[47] Given d, S, and h_c for each coral species, the model geometry parameters λ_f and λ_p are first calculated using equations (9) and (10), respectively. Equations (24) and (26) are then used to calculate inertia-dominated and unidirectional flow limits α_i and α_c, respectively. The ratios α_i/α_c are listed in Table 4, which according to equation (29) represents the maximum possible oscillatory flow enhancement. Values of α_i/α_c are high for all coral species, indicating that surface waves have the ability to significantly increase flow within these canopies by roughly one order of magnitude.

[48] Although the ratio α_i/α_c provides an estimate of the maximum oscillatory flow enhancement, the actual enhancement α_w/α_c for each coral will be determined by properties of the waves, and in particular on the magnitude of A_∞^{rms}. Reef organisms can experience a wide range of wave conditions depending on the environment in which they live. For example, the coral community in Figure 1a experiences typical near-bed wave orbital velocities of $U_{\infty,w}^{rms} = 30$ cm/s with 7 second periods [*Lowe et al.*, 2005a], corresponding to $A_\infty^{rms} = 30$ cm. As another example, consider a reef located at a depth $h = 5$ m exposed to 7 second period waves. The depth-limited maximum possible wave height at this site would be roughly $0.4h = 2$ m [*Thornton and Guza*, 1982] which would correspond to $A_\infty^{rms} = 130$ cm. In general, it is reasonable to assume that the vast majority of reef organisms are exposed to conditions where A_∞^{rms} is order 100 cm or less. Therefore, for each coral listed in Table 4, α_w is calculated by solving equation (22) for values of $A_{\infty,w}^{rms} = 1$, 10 and 100 cm. For each species, the model predicts oscillatory flow enhancements α_w/α_c ranging from

roughly 10 for A_∞^{rms} = 1 cm to 3 when A_∞^{rms} = 100 cm. These results confirm that oscillatory flow generated by surface waves should significantly increase water motion inside these coral canopies for the full range of wave conditions experienced by these organisms.

6. Summary and Conclusions

[49] Theory developed in section 2 showed that oscillatory flow generated by surface waves always generates higher in-canopy flow when compared to a unidirectional current of the same magnitude. The particular degree of oscillatory flow enhancement was found to be governed by three dimensionless parameters that depend on the particular geometry of the canopy and the wave conditions. Depending on the magnitude of these parameters, the flow falls into one of three possible flow regimes. For cases where the wave orbital excursion length A_∞^{rms} is small relative to the canopy drag and shear length scales, L_d and L_s respectively, resistance to flow inside the canopy is provided by the inertia force generated by the interaction of the canopy elements with the accelerating in-canopy flow. This inertia force is a unique feature of oscillatory canopy flows. In the other extreme where A_∞^{rms} is large, the in-canopy flow approaches a unidirectional limit. Between the inertia and unidirectional limits is a general flow region where the in-canopy flow decreases with increasing A_∞^{rms}. Results from the unidirectional and wave experiments were all predicted well using this theory. However, due to limits of the flume and wavemaker, for all wave experiments the in-canopy flow was always inertia force dominated. Therefore the theory has been shown to work well to predict the in-canopy flow at these inertia-dominated and unidirectional limits.

[50] The notion that waves have the potential to increase flow inside canopies derived from benthic organisms clearly has important ecological implications. Many of these canopies, such as the example of the coral canopies discussed in section 5, are located in environments with significant wave activity where waves are expected to significantly enhance in-canopy water motion. For unidirectional flow, many biological processes such as nutrient uptake have previously been shown to increase as the flow velocity increases. Although, relatively little is known about role of waves on many of these biological processes, results from this study indicate that surface waves have the ability to influence and perhaps dominate many of these processes due to the higher in-canopy flow they generate. In the subsequent paper by *Lowe et al.* [2005b], the effect of oscillatory flow on canopy mass transfer is specifically investigated.

Appendix A: Numerical Solution of the Canopy Flow Equation

[51] To solve for the in-canopy velocity, equation (22) is solved numerically using the following method. The equation is rewritten as

$$(1+C)\frac{\partial \widehat{U}_w^*}{\partial t^*} = A\left|U_{\infty,w}^*\right|U_{\infty,w}^* - B\left|\widehat{U}_w^*\right|\widehat{U}_w^* + \frac{\partial U_{\infty,w}^*}{\partial t^*}, \quad \text{(A1)}$$

where

$$A = \frac{A_\infty^{rms}}{L_s}, \quad B = \frac{A_\infty^{rms}}{L_d}, \quad C = \frac{C_M \lambda_p}{1-\lambda_p}. \quad \text{(A2)}$$

The forcing term $U_{\infty,w}^*$ is known and is provided by equation (3):

$$U_{\infty,w}^* = \sqrt{2}\cos(t_*), \quad \text{(A3)}$$

where the $\sqrt{2}$ term is included since for the sinusoidal velocity in equation (3), the rms velocity $U_{\infty,w}^{rms}$ is

$$U_{\infty,w}^{rms} = \frac{1}{\sqrt{2}} U_{\infty,w}^{\max}.$$

Equation (A1) is discretized using forward differencing:

$$(1+C)\left[\frac{\widehat{U}_w^{*(i+1)} - \widehat{U}_w^{*(i)}}{\Delta t}\right] = A\left|U_{\infty,w}^{*(i)}\right|U_{\infty,w}^{*(i+1)} - B\left|\widehat{U}_w^{*(i)}\right|\widehat{U}_w^{*(i+1)} + \frac{\partial U_{\infty,w}^{*(i)}}{\partial t^*}, \quad \text{(A4)}$$

where Δt refers to the time step size, and i refers to the step number. Note that the quadratic nonlinear terms have been linearized by staggering the step numbers on these terms. Equation (A4) can be rearranged to give

$$\widehat{U}_w^{*(i+1)} = \frac{1}{D}\left[\frac{(1+C)}{\Delta t}\widehat{U}_w^{*(i)} + A\left|U_{\infty,w}^{*(i)}\right|U_{\infty,w}^{*(i+1)} + \frac{\partial U_{\infty,w}^{*(i)}}{\partial t^*}\right], \quad \text{(A5)}$$

where

$$D = \frac{(1+C)}{\Delta t} + B\left|U_w^{*(i)}\right|. \quad \text{(A6)}$$

Equation (A5) is solved by providing an initial condition and marching forward in time. Since the initial condition is not exactly known beforehand, the solution is advanced for several wave periods until a quasi-steady state is reach. This was generally attained after only one wave period. Finally, $\widehat{U}_w^{\text{rms}}$ and $U_{\infty,w}^{\text{rms}}$ were calculated using equations (5) and (6), which allowed the canopy attenuation parameter α_w to be calculated using equation (8).

Notation

a	surface wave amplitude.
A_f	canopy element frontal area.
A_p	canopy element plan area.
A_T	area of repeating canopy element unit.
A_∞^{rms}	rms wave orbital excursion length.
C_d	sectional canopy drag coefficient.
C_{dh}	drag coefficient based on velocity at $z = h_c$.
C_f	canopy friction coefficient.
C_M	canopy inertia force coefficient.
d	cylinder diameter.
f	canopy resistance force.

f_d canopy drag force.
f_i canopy inertia force.
g gravitational acceleration.
h water depth.
h_c canopy height.
k wave number.
L_d canopy drag length scale.
L_s canopy shear length scale.
P pressure field.
S canopy element spacing.
t time.
T wave period.
u instantaneous velocity in x direction.
u' turbulent velocity fluctuation in x direction.
u'' spatial velocity deviation.
u_* friction velocity based on canopy shear stress.
U combined wave-current flow velocity.
U_c time-averaged current profile.
U_w phase-varying oscillatory velocity profile.
$U_{\infty,c}$ free-stream current velocity.
$U_{\infty,w}$ free-stream oscillatory velocity.
w instantaneous velocity in z direction.
w' turbulent velocity fluctuation in z direction.
x streamwise direction.
x_o canopy flow development length.
y cross stream direction.
z vertical elevation measured from canopy base.
α_c unidirectional canopy flow attenuation parameter.
α_w oscillatory canopy flow attenuation parameter.
α_i attenuation parameter for inertia dominated flow.
λ wave length.
λ_f frontal area canopy geometry parameter.
λ_p plan area canopy geometry parameter.
τ shear stress.
ρ fluid density.
ω radian wave frequency.

Subscripts

c parameter associated with current.
w parameter associated with oscillatory flow.

Superscripts

max velocity amplitude.
rms root mean squared velocity (rms).
* dimensionless variable.

Other

$\wedge$ overhat denoting canopy depth-averaged velocity.
$\langle\ \rangle$ spatial average operator.
$-$ overbar denoting time average operator.
$|\ |$ absolute value.

[52] **Acknowledgments.** We thank Uri Shavit and two anonymous reviewers for providing helpful comments on this manuscript. This work was supported by the National Science Foundation under grant OCE-0117859.

References

Batchelor, G. (1967), *An Introduction to Fluid Mechanics*, Cambridge Univ. Press, New York.

Belcher, S. E., N. Jerram, and J. C. R. Hunt (2003), Adjustment of a turbulent boundary layer to a canopy of roughness elements, *J. Fluid Mech.*, *488*, 369–398.

Bentham, T., and R. Britter (2003), Spatially averaged flow within obstacle arrays, *Atmos. Environ.*, *37*(15), 2037–2043.

Bilger, R. W., and M. J. Atkinson (1992), Anomalous mass transfer of phosphate on coral reef flats, *Limnol. Oceanogr.*, *37*(2), 261–272.

Britter, R., and S. Hanna (2003), Flow and dispersion in urban areas, *Ann. Rev. Fluid Mech.*, *35*, 469–496.

Brunet, Y., J. J. Finnigan, and M. R. Raupach (1994), A wind-tunnel study of air-flow in waving wheat—Single-point velocity statistics, *Boundary Layer Meteorol.*, *70*(1–2), 95–132.

Carpenter, R. C., J. M. Hackney, and W. H. Adey (1991), Measurements of primary productivity and nitrogenase activity of coral-reef algae in a chamber incorporating oscillatory flow, *Limnol. Oceanogr.*, *36*(1), 40–49.

Chamberlain, J. A., and R. R. Graus (1975), Water-flow and hydromechanical adaptations of branched reef corals, *Bull. Mar. Sci.*, *25*(1), 112–125.

Cheng, H., and I. P. Castro (2002), Near wall flow over urban-like roughness, *Boundary Layer Meteorol.*, *104*(2), 229–259.

Coceal, O., and S. Belcher (2004), A canopy model of mean winds through urban areas, *Q. J. R. Meteorol. Soc.*, *130*, 1349–1372.

Crimaldi, J. P., J. K. Thompson, J. H. Rosman, R. J. Lowe, and J. R. Koseff (2002), Hydrodynamics of larval settlement: The influence of turbulent stress events at potential recruitment sites, *Limnol. Oceanogr.*, *47*(4), 1137–1151.

Dean, R., and R. Dalrymple (1991), *Water Wave Mechanics for Engineers and Scientists*, vol. 2, *Adv. Ser. on Ocean Eng.*, vol. 2, World Sci., Tokyo.

Falter, J. L., M. J. Atkinson, and M. Merrifield (2004), Mass transfer limitation of nutrient uptake by a wave-dominated reef flat community, *Limnol. Oceanogr.*, *49*, 1820–1831.

Falter, J. L., M. Atkinson, and C. Coimbra (2005), Effects of surface roughness and oscillatory flow on the dissolution of plaster forms: Evidence for nutrient mass transfer to coral reef communities, *Limnol. Oceanogr.*, *50*(1), 246–254.

Finnigan, J. (2000), Turbulence in plant canopies, *Ann. Rev. Fluid Mech.*, *32*, 519–571.

Ghisalberti, M., and H. M. Nepf (2002), Mixing layers and coherent structures in vegetated aquatic flows, *J. Geophys. Res.*, *107*(C2), 3011, doi:10.1029/2001JC000871.

Ghisalberti, M., and H. M. Nepf (2004), The limited growth of vegetated shear layers, *Water Resour. Res.*, *40*, W07502, doi:10.1029/2003WR002776.

Grant, W. D., and O. S. Madsen (1986), The continental-shelf bottom boundary-layer, *Ann. Rev. Fluid Mech.*, *18*, 265–305.

Grimmond, C., and T. Oke (1999), Aerodynamic properties of urban areas derived from analysis of surface form, *J. Appl. Meteorol.*, *38*, 1262–1292.

Hearn, C. J., M. J. Atkinson, and J. L. Falter (2001), A physical derivation of nutrient-uptake rates in coral reefs: Effects of roughness and waves, *Coral Reefs*, *20*(4), 347–356.

Helmuth, B. S. T., K. P. Sebens, and T. L. Daniel (1997), Morphological variation in coral aggregations: Branch spacing and mass flux to coral tissues, *J. Experimen. Mar. Biol. Ecol.*, *209*(1–2), 233–259.

Hurd, C. L. (2000), Water motion, marine macroalgal physiology, and production, *J. Phycol.*, *36*(3), 453–472.

Kastner-Klein, P., and M. Rotach (2004), Mean flow and turbulence characteristics in an urban roughness sublayer, *Boundary Layer Meteorol.*, *111*, 55–84.

Koch, E. W. (1994), Hydrodynamics, diffusion-boundary layers and photosynthesis of the seagrasses Thalassia-testudinum and Cymodocea-nodosa, *Mar. Biol.*, *118*(4), 767–776.

Lesser, M. P., V. M. Weis, M. R. Patterson, and P. L. Jokiel (1994), Effects of morphology and water motion on carbon delivery and productivity in the reef coral, Pocillopora-damicornis (Linnaeus)—Diffusion-barriers, inorganic carbon limitation, and biochemical plasticity, *J. Experiment. Mar. Biol. Ecol.*, *178*(2), 153–179.

Lodahl, C. R., B. M. Sumer, and J. Fredsoe (1998), Turbulent combined oscillatory flow and current in a pipe, *J. Fluid Mech.*, *373*, 313–348.

Lowe, R. J., J. L. Falter, M. D. Bandet, G. Pawlak, M. J. Atkinson, S. G. Monismith, and J. R. Koseff (2005a), Spectral wave dissipation over a barrier reef, *J. Geophys. Res.*, *110*, C04001, doi:10.1029/2004JC002711.

Lowe, R. J., J. R. Koseff, S. G. Monismith, and J. L. Falter (2005b), Oscillatory flow through submerged canopies: 2. Canopy mass transfer, *J. Geophys. Res.*, *110*, C10017, doi:10.1029/2004JC002789.

Macdonald, R. (2000), Modelling the mean velocity in the urban canopy layer, *Boundary Layer Meteorol.*, *97*, 25–45.

Marshall, P. A. (2000), Skeletal damage in reef corals: relating resistance to colony morphology, *Mar. Ecol. Prog. Ser.*, *200*, 177–189.

Nepf, H. M., and E. R. Vivoni (2000), Flow structure in depth-limited, vegetated flow, *J. Geophys. Res.*, *105*(C12), 28,547–28,557.
Nielsen, P. (1992), *Coastal Bottom Boundary Layers and Sediment Transport*, vol. 4, *Adv. Ser. Ocean Eng.*, World Sci., Tokyo.
Pidgeon, E. J. (1999), An experimental investigation of breaking wave induced turbulence, PhD thesis, Stanford Univ., Stanford, Calif.
Poggi, D., A. Porporato, L. Ridolfi, J. Albertson, and G. Katul (2004), The effect of vegetation density on canopy sub-layer turbulence, *Boundary Layer Meteorol.*, *111*, 565–587.
Raupach, M. R., and R. H. Shaw (1982), Averaging procedures for flow within vegetation canopies, *Boundary Layer Meteorol.*, *22*(1), 79–90.
Reed, D. C., T. W. Anderson, A. W. Ebeling, and M. Anghera (1997), The role of reproductive synchrony in the colonization potential of kelp, *Ecology*, *78*(8), 2443–2457.
Reidenbach, M. A., J. R. Koseff, S. G. Monismith, J. V. Steinbuck, and A. Genin (2005), The effects of waves and morphology on mass transfer within branched reef corals, *Limnol. Oceanogr.*, in press.
Schlichting, H., and K. Gersten (2000), *Boundary Layer Theory*, Springer, New York.
Thomas, F. I. M., and M. J. Atkinson (1997), Ammonium uptake by coral reefs: Effects of water velocity and surface roughness on mass transfer, *Limnol. Oceanogr.*, *42*(1), 81–88.
Thomas, F. I. M., and C. D. Cornelisen (2003), Ammonium uptake by seagrass communities: Effects of oscillatory versus unidirectional flow, *Mar. Ecol. Prog. Ser.*, *247*, 51–57.
Thomas, F. I. M., C. D. Cornelisen, and J. M. Zande (2000), Effects of water velocity and canopy morphology on ammonium uptake by seagrass communities, *Ecology*, *81*(10), 2704–2713.
Thornton, E. B., and R. T. Guza (1982), Energy saturation and phase speeds measured on a natural beach, *J. Geophys. Res.*, *87*, 9499–9508.
Wildish, D., and D. Kristmanson (1997), *Benthic Suspension Feeders and Flow*, Cambridge Univ. Press, New York.

J. R. Koseff, R. J. Lowe, and S. G. Monismith, Department of Civil and Environmental Engineering, Stanford University, Environmental Fluid Mechanics Laboratory, Stanford, CA 94305-4020, USA. (rlowe@stanford.edu)